Journal of Applied Electrochemistry **30**: 135–146, 2000.

Three-dimensional numerical simulation of straight channel PEM fuel cells

S. DUTTA[1]*, S. SHIMPALEE[1] and J.W. VAN ZEE[2]
[1]*Department of Mechanical Engineering and*
[2]*Department of Chemical Engineering, University of South Carolina, Columbia, SC 29208, USA*
*(*author for correspondence, e-mail: dutta@engr.sc.edu; fax: +1 803 777 0106)*

Received 24 March 1999; accepted in revised form 8 July 1999

Key words: current distribution, fuel cell, mass transfer, PEM

Abstract

The need to model three-dimensional flow in polymer electrolyte membrane (PEM) fuel cells is discussed by developing an integrated flow and current density model to predict current density distributions in two dimensions on the membrane in a straight channel PEM fuel cell. The geometrical model includes diffusion layers on both the anode and cathode sides and the numerical model solves the same primary flow related variables in the main flow channel and the diffusion layer. A control volume approach is used and source terms for transport equations are presented to facilitate their incorporation in commercial flow solvers. Predictions reveal that the inclusion of a diffusion layer creates a lower and more uniform current density compared to cases without diffusion layers. The results also show that the membrane thickness and cell voltage have a significant effect on the axial distribution of the current density and net rate of water transport. The predictions of the water transport between cathode and anode across the width of the flow channel show the delicate balance of diffusion and electroosmosis and their effect on the current distribution along channel.

List of symbols

a_K	activity of water in stream K (dimensionless)
A_{cv}	specific surface area of the control volume (c.v.) (m^{-1})
C_{wK}	concentration of water at K interface of the membrane (mol m^{-3})
$D_{i,j}$	pseudo binary diffusion coefficient of species i in mixture j ($m^2\ s^{-1}$)
D_w	diffusion coefficient of water ($m^2\ s^{-1}$)
F	Faraday constant (96 487 C mol^{-1})
I	local current density (A m^{-2})
I_o	exchange current density for the oxygen reaction (100 A m^{-2})
$m_{K,l}$	mass fraction of the species l in stream K (dimensionless)
$M_{m,dry}$	equivalent weight of a dry membrane (kg mol^{-1})
M_{H_2}	molecular weight of hydrogen (kg mol^{-1})
M_{O_2}	molecular weight of oxygen (kg mol^{-1})
n_d	electroosmotic drag coefficient (number of water molecules carried per proton)
$P^{sat}_{w,K}$	vapour pressure of water in stream K (Pa)
P	total pressure (Pa)
P_{O_2}	partial pressure of oxygen (Pa)
R	universal gas constant (8.314 J $mol^{-1}\ K^{-1}$)
t_m	membrane thickness (m)
T_s	surface temperature at the anode (K)
u, v, w	velocities in x, y and z directions, respectively (m s^{-1})
V_{oc}	cell open-circuit voltage (V)
V_{cell}	cell voltage (V)
x	channel length measured from anode inlet (m)
$X_{w,K}$	mole fraction of water in stream K

Greek symbols

μ	dynamic viscosity (kg s m^{-2})
α	net water flux per proton flux
η	overpotential for oxygen reaction (V)
σ_m	membrane conductivity ($\Omega^{-1}\ m^{-1}$)
$\rho_{m,dry}$	density of a dry membrane (kg m^{-3})
ρ	density of the mixture (kg m^{-3})
β_ξ	permeability in the ξ direction

Subscripts/superscripts

a	anode
c	cathode
H_2	hydrogen
K	anode or cathode
O_2	oxygen
w	water
sat	saturated
ξ	dummy variable for direction x, y or z

1. Introduction

Polymer electrolyte membrane (PEM) fuel cells use gas diffusion layers to enhance the reaction area accessible by the reactants. The effect of using these diffusion layers is to allow a spatial distribution in the current density on the membrane in both the direction of bulk flow and the direction orthogonal to the flow but parallel to the membrane. Recently, experimental measurements of this distribution were reported [1, 2]. This two-dimensional distribution cannot be modelled with the well-used one and two-dimensional models such as those shown in Refs. [3–7]. Even an alternative to these models recently published by Gurau et al. [8] in which they solve a set of two-dimensional flow equations in the channel and the gas diffusion layer cannot map the distribution because they ignore the width of the flow channel. Here, we report a numerical model that includes the full three-dimension solution to the Navier–Stokes equations for the flow channel. This three-dimensional analysis allows one to account for the effect of the width of the flow channel on the velocity distribution. In this paper we show how to modify a commercially available computational fluids code, Fluent (Fluent, Inc., Lebanon, NH, USA), to account for electrochemical reactions and we use this code to predict the current density and water transport in a straight channel fuel cell. We discuss how the mass consumed in the electrochemical reactions affects the momentum transport equations. We show that under certain conditions the transport towards the membrane is driven by both the pressure and concentration gradients rather than by diffusion alone.

Previous studies [3–6] have focused on two dimensions of the fuel cell: one direction parallel to the membrane in the direction of bulk flow and the other direction across the membrane. Only a few models included two-dimensional transport of the reactants and products in the flow channels [7, 8]. The model presented by Springer et al. [3] prepared the foundation for these simulations by also providing the key properties of the membrane required for a numerical model. They considered a pseudo one-dimensional model in which flow channels were treated as being well mixed. Later, Fuller and Newman [4] and Nguyen and White [5] developed two-dimensional heat and water transport models that accounted for variation in temperature and membrane hydration conditions along the flow channels. Both of these models assumed a well-mixed concentration in the flow channel. Fuller and Newman [4] included the diffusion layer for water transport but Nguyen and White [5] neglected the diffusion layer. Nguyen and White [5] investigated the effectiveness of various humidification systems in maintaining a high degree of membrane hydration and performance for PEM fuel cells. Recently, Yi and Nguyen [6] modified the previous models to include both the liquid and gas phase along the flow path of both anode and cathode sides of a PEM fuel cell. As a further extension of these models, Gurau et al. [8] included two-dimensional fluid flow in the channels but the density change due to species consumption appears to be neglected. Moreover, the connectivity of the main channel and diffusion layer involved a change of primary variables that may lead to numerical discontinuities under some operating conditions.

Another recent numerical prediction by Yi and Nguyen [7] analysed the two-dimensional hydrodynamics in only the cathode. In both [7] and [8] the width of the channel and the portion of the gas diffusion layer hidden from the channel were neglected. As shown below, these previous models provide a reasonable prediction of the axial water distribution but they overestimate the nonuniformity of the current distribution at the entrance of a PEM fuel cell. By using the 'Fluent code' as the flow solver, we overcome the main difficulty in including the third spatial dimension. That is, we allow the commercially proven and readily accessible flow solver to develop and converge the source code that becomes significantly more complicated in three dimensions.

In this work a numerical model is developed to understand gas flow and species transport in a fuel cell. The complete three-dimensional Navier–Stokes equations are solved with a control volume based discretization of the computation domain to obtain the velocity and pressure distribution in the flow channels and the gas diffusion layer. The mass flow conditions inside the system, such as the concentration of the species along the flow channel and water activity at the anode in the two dimensions of the membrane are determined. This three-dimensional analysis provides the distributions that cannot be achieved with two-dimensional simulations.

2. Model development

Figure 1 shows the schematic of the cell construction and the species flow in a typical PEM fuel cell. The model regions consist of two distinct flow channels separated by the membrane and electrode assembly (MEA); one channel is for the anode gases and the other is for the cathode gases. In between the flow channels and the MEA there are two diffusion layers. This

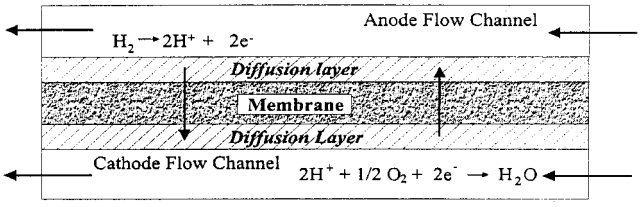

Fig. 1. Schematic of the anode and cathode flow channels in a PEM fuel cell showing the transport of H^+ to the cathode and the possibility of back diffusion of water from the cathode to the anode. Note that there is significant transport of water from the anode to the cathode by electroosmosis.

numerical model assumes steady state, isothermal and single-phase behaviour and it is the first to predict the three-dimensional aspects of a PEM fuel cell. We use the assumption of steady state to compare with the predictions of previous work. We have used the assumption of isothermal conditions to compare with data [9] because in our experimental fuel cells the thermal inertia of the graphite current collectors is large to prevent temperature variations. This assumption can be relaxed by using the appropriate equations published in the two-dimensional models of [4] and [6]. The model converts the electrochemical aspects of governing differential equations in [4] and [6] to source terms that are usable for the control volume analysis. Fluent then solves the complete Navier–Stokes flow equations with our source terms. The effect of the membrane thickness and the cell voltage on the local current density, the net water flux per proton, and the secondary flow along the channel are studied for different inlet conditions. Our results are compared with the original base case solutions of [4] and [6] to illustrate the influence of the three-dimensional flow and diffusion layer that are added in this study.

The computation domain, as shown in Figure 2, is composed of the anode flow channel, anode diffusion layer, MEA, cathode diffusion layer, and cathode flow channel. Figure 2 also shows the grid arrangement used. We consider five species, which are hydrogen, oxygen, carbon dioxide, nitrogen and water vapour. The fuel cell

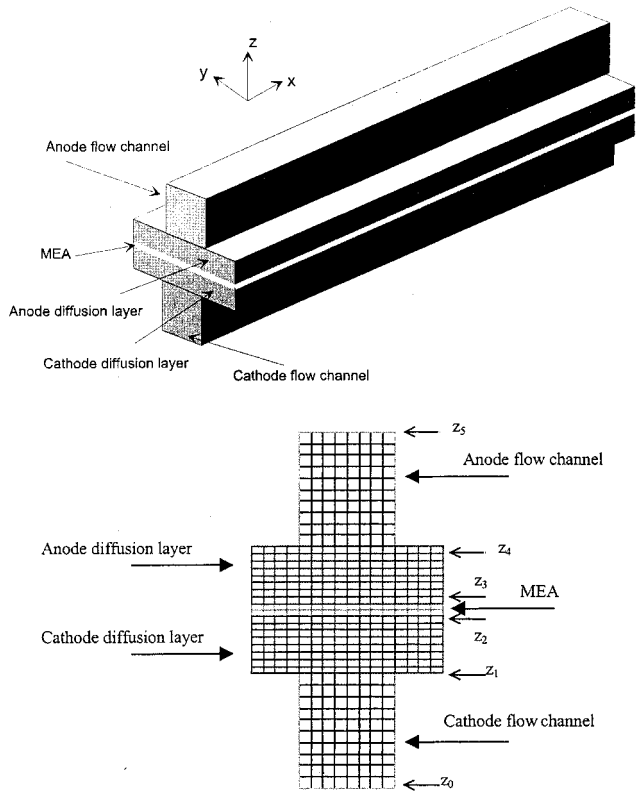

Fig. 2. Schematic of the computation domain for a straight channel fuel cell with diffusion layers in the anode and cathode sides of the membrane electrode assembly (MEA). A typical cross section of the domain and the location of diffusion layers are also shown.

operation is characterized as gas transport and transformation of one species to the other. The hydrogen from the anode flow channel is transported through the diffusion layer toward the membrane. Hydrogen molecules are dissociated to protons and electrons in the catalyst as shown in Figure 1. The water that impregnates the MEA hydrates the protons and it is transported by both electroosmosis and diffusion. The air mixture in the cathode channel is transported through the diffusion layer toward the membrane where oxygen reacts with protons as also shown in Figure 1. The water activity in the membrane is simulated by surface based source terms in the control volumes in contact with the membrane.

2.1. *Model equations*

The conservation of mass equation (Table 1, Equation 1) in the three-dimensional flow solver software, Fluent, is modified to include the electrochemical aspects of a fuel cell by using the respective source terms, S_m, shown by Equations 7 and 9–12 of Table 1. Equations for source terms are given as volumetric, that is, these source terms are defined per unit volume of the computational control volumes. The source terms are zero in most of the computation domain. These terms corresponds to the consumption of hydrogen in the anode, and the consumption of oxygen and production of water in the cathode. The flux of water is also included as a source term at the anode and cathode (i.e., Equations 10 and 12) by accounting for the diffusion and electroosmotic drag as defined by Equations 15 and 16 of Table 2.

The momentum transport equation has a source term for the porous media used for flows through diffusion layer based on Darcy's law [10]. The addition of this source term effectively converts the momentum equation in the x-direction to $\partial P/\partial x = -(\mu/\beta_x)u$ in the porous layer because β_x is very small and thus the other terms become negligible. A pressure drop is created in the porous layer that is proportional to the mixture velocity in the cell. This source term removes the need for a change in the flow variable shown in the model of [8]. The permeability, β_ξ, is assumed to be isotropic and was calculated to be 2.0×10^{-10} m^2 [6] (porosity of 0.7) and 2.3×10^{-11} m^2 [4] (porosity of 0.4).

The species transport equations (Equations 3–6 of Table 1) are solved for the mass flow rates of the hydrogen, water and oxygen species based on the mixture velocities, u, v and w, and the diffusion mass fluxes $J_{\xi,l}$. The species binary diffusion coefficients are calculated as shown by Equation 14 in Table 2. There is one inert component on each side and the concentration of each was determined from a summation of the mass fractions of the other species. Fuller and Newman integrate the flux expression for the diffusion of water through the membrane whereas [5–7] assumed a linear gradient as shown by Equation 15. The diffusion coefficient of each species in the mixture was reduced

Table 1. Governing equations and source terms

Governing equations	Mathematical expressions		Nonzero volumetric source terms and location of application (Fig. 2)	
Conservation of mass	$\frac{\partial(\rho u)}{\partial x}+\frac{\partial(\rho v)}{\partial y}+\frac{\partial(\rho w)}{\partial z}=S_{\mathrm{m}}$	(1)	$S_{\mathrm{m}}=S_{\mathrm{H_2}}+S_{\mathrm{aw}}$ at $z=z_3$ $S_{\mathrm{m}}=S_{\mathrm{O_2}}+S_{\mathrm{cw}}$ at $z=z_2$	(7)
Momentum transport	$u\frac{\partial(\rho u)}{\partial x}+v\frac{\partial(\rho u)}{\partial y}+w\frac{\partial(\rho u)}{\partial z}=-\frac{\partial P}{\partial x}+\frac{\partial}{\partial x}\left(\mu\frac{\partial u}{\partial x}\right)+\frac{\partial}{\partial y}\left(\mu\frac{\partial u}{\partial y}\right)+\frac{\partial}{\partial z}\left(\mu\frac{\partial u}{\partial z}\right)+S_{\mathrm{px}}$ $u\frac{\partial(\rho v)}{\partial x}+v\frac{\partial(\rho v)}{\partial y}+w\frac{\partial(\rho v)}{\partial z}=-\frac{\partial P}{\partial y}+\frac{\partial}{\partial x}\left(\mu\frac{\partial v}{\partial x}\right)+\frac{\partial}{\partial y}\left(\mu\frac{\partial v}{\partial y}\right)+\frac{\partial}{\partial z}\left(\mu\frac{\partial v}{\partial z}\right)+S_{\mathrm{py}}$ $u\frac{\partial(\rho w)}{\partial x}+v\frac{\partial(\rho w)}{\partial y}+w\frac{\partial(\rho w)}{\partial z}=-\frac{\partial P}{\partial z}+\frac{\partial}{\partial x}\left(\mu\frac{\partial w}{\partial x}\right)+\frac{\partial}{\partial y}\left(\mu\frac{\partial w}{\partial y}\right)+\frac{\partial}{\partial z}\left(\mu\frac{\partial w}{\partial z}\right)+S_{\mathrm{pz}}$	(2)	$S_{\mathrm{px}}=-\frac{\mu u}{\beta_x}$; $S_{\mathrm{py}}=-\frac{\mu v}{\beta_y}$; $S_{\mathrm{pz}}=-\frac{\mu w}{\beta_z}$ at $z_1\le z\le z_4$	(8)
Hydrogen transport (anode side)	$u\frac{\partial(\rho m_{\mathrm{H_2}})}{\partial x}+v\frac{\partial(\rho m_{\mathrm{H_2}})}{\partial y}+w\frac{\partial(\rho m_{\mathrm{H_2}})}{\partial z}=\frac{\partial(J_{x,\mathrm{H_2}})}{\partial x}+\frac{\partial(J_{y,\mathrm{H_2}})}{\partial y}+\frac{\partial(J_{z,\mathrm{H_2}})}{\partial z}+S_{\mathrm{H_2}}$	(3)	$S_{\mathrm{H_2}}=-\frac{I(x,y)}{2F}M_{\mathrm{H_2}}A_{\mathrm{cv}}$ at $z=z_3$	(9)
Water transport (anode side)	$u\frac{\partial(\rho m_{\mathrm{aw}})}{\partial x}+v\frac{\partial(\rho m_{\mathrm{aw}})}{\partial y}+w\frac{\partial(\rho m_{\mathrm{aw}})}{\partial z}=\frac{\partial(J_{x,\mathrm{aw}})}{\partial x}+\frac{\partial(J_{y,\mathrm{aw}})}{\partial y}+\frac{\partial(J_{z,\mathrm{aw}})}{\partial z}+S_{\mathrm{aw}}$	(4)	$S_{\mathrm{aw}}=-\frac{\alpha(x,y)}{F}I(x,y)M_{\mathrm{H_2O}}A_{\mathrm{cv}}$ at $z=z_3$	(10)
Oxygen transport (cathode side)	$u\frac{\partial(\rho m_{\mathrm{O_2}})}{\partial x}+v\frac{\partial(\rho m_{\mathrm{O_2}})}{\partial y}+w\frac{\partial(\rho m_{\mathrm{O_2}})}{\partial z}=\frac{\partial(J_{x,\mathrm{O_2}})}{\partial x}+\frac{\partial(J_{y,\mathrm{O_2}})}{\partial y}+\frac{\partial(J_{z,\mathrm{O_2}})}{\partial z}+S_{\mathrm{O_2}}$	(5)	$S_{\mathrm{O_2}}=-\frac{I(x,y)}{4F}M_{\mathrm{O_2}}A_{\mathrm{cv}}$ at $z=z_2$	(11)
Water transport (cathode side)	$u\frac{\partial(\rho m_{\mathrm{cw}})}{\partial x}+v\frac{\partial(\rho m_{\mathrm{cw}})}{\partial y}+w\frac{\partial(\rho m_{\mathrm{cw}})}{\partial z}=\frac{\partial(J_{x,\mathrm{cw}})}{\partial x}+\frac{\partial(J_{y,\mathrm{cw}})}{\partial y}+\frac{\partial(J_{z,\mathrm{cw}})}{\partial z}+S_{\mathrm{cw}}$	(6)	$S_{\mathrm{cw}}=\frac{1+2\alpha(x,y)}{2F}I(x,y)M_{\mathrm{H_2O}}A_{\mathrm{cv}}$ at $z=z_2$	(12)

Table 2. Equations for modelling electrochemical effects

Diffusion mass flux of species l in ξ direction	$J_{i,l} = -\rho D_{i,l} \dfrac{\partial m_{K,l}}{\partial \xi}$	(13)
Binary diffusion coefficient [10]	$\dfrac{PD_{i,j}(x,y)}{(P_{c-i} \times P_{c-j})^{1/3} \times (T_{c-i}T_{c-j})^{5/12} \times \left(\frac{1}{M_i} + \frac{1}{M_j}\right)^{1/2}} = 3.64 \times 10^{-8} \left(\dfrac{T_{\text{cell}}}{\sqrt{T_{c-i}T_{c-j}}}\right)^{2.334}$	(14)
Net water transfer coefficient per proton	$\alpha(x,y) = n_{\text{d}}(x,y) - \dfrac{F}{I(x,y)} D_{\text{W}}(x,y) \left(\dfrac{C_{\text{wc}}(x,y) - C_{\text{wa}}(x,y)}{t_{\text{m}}}\right)$	(15)
Electroosmotic drag coefficient	$n_{\text{d}}(x,y) = 0.0049 + 2.02a_{\text{a}} - 4.53a_{\text{a}}^2 + 4.09a_{\text{a}}^3;\ a_{\text{a}} \le 1$ $= 1.59 + 0.159(a_{\text{a}} - 1);\ a_{\text{a}} > 1$	(16)
Water diffusion coefficient for cases similar to Yi and Nguyen [6]	$D_{\text{W}} = n_{\text{d}} 5.5 \times 10^{-11} \exp\left[2416\left(\dfrac{1}{303} - \dfrac{1}{T_{\text{s}}}\right)\right]$	(17)
Water diffusion coefficient for cases similar to Fuller and Newman [4]	$D_{\text{W}} = 3.5 \times 10^{-6} \lambda \exp\left(-\dfrac{2436}{T_{\text{s}}}\right)$	(18)
Water concentration for anode and cathode surfaces of the MEA	$C_{\text{w}K}(x,y) = \dfrac{\rho_{\text{m,dry}}}{M_{\text{m,dry}}}(0.043 + 17.8a_K - 39.8a_K^2 + 36.0a_K^3);\ a_K \le 1$ $= \dfrac{\rho_{\text{m,dry}}}{M_{\text{m,dry}}}(14 + 1.4(a_K - 1));\ \text{for } a_K > 1,\ \text{where } K = a \text{ or } c$	(19)
Water activity	$a_K = \dfrac{X_{\text{w},K} P(x,y)}{P_{\text{w},K}^{\text{sat}}}$	(20)
Local current density	$I(x,y) = \dfrac{\sigma_{\text{m}}(x,y)}{t_{\text{m}}} \{V_{\text{oc}} - V_{\text{cell}} - \eta(x,y)\}$	(21)
Local membrane conductivity	$\sigma_{\text{m}}(x,y) = \left(0.005\,14 \dfrac{M_{\text{m,dry}}}{\rho_{\text{m,dry}}} C_{\text{wa}}(x,y) - 0.003\,26\right) \exp\left(1268\left(\dfrac{1}{303} - \dfrac{1}{T_{\text{s}}}\right)\right) \times 10^2$	(22)
Local overpotential	$\eta(x,y) = \dfrac{RT_{\text{s}}}{0.5F} \ln\left(\dfrac{I(x,y)}{I_0 P_{\text{O}_2}(x,y)}\right)$	(23)

arbitrarily by 50% in the diffusion layer to account for the effect of porosity and pore-tortuosity. The flux of water through the membrane is critical to the predictions and here we have used the same equations for electroosmotic drag and water diffusion coefficients as previous workers so that the predictions can be compared (Table 2). The diffusion coefficient of Fuller and Newman [4] is dependent on the local λ, and since we used Equation 15 to compare with [6] we based our diffusion coefficient for comparison with [4] on the local λ values taken from the profiles given in [4].

The expressions for water concentration at the anode and cathode sides, $C_{\text{w,a}}$ and $C_{\text{w,c}}$, are calculated according to Equation 19 and the activity of water is also defined in Table 2. The source terms in Table 1 correspond to the control volume and not the boundary conditions at the anode or cathode interfaces. For the correct determination of the concentrations and activities at the membrane–diffusion layer interface, the mole fraction for each species used in these equations must be extrapolated to the membrane surface. We used linear extrapolation with the grid of Figure 2 and achieved a grid independent solution.

Several assumptions are made in this study. The flow is assumed to be isothermal and water transport in the flow channels is assumed to occur in vapour form. The electrical resistance of the electrodes is assumed to be negligible. The hydrogen oxidation is assumed to be facile and chemical reactions are assumed to be perfect. No internal activities occurring inside the MEA are modeled in detail.

2.2. *Numerical procedure*

A control volume technique based on a commercial flow solver, Fluent (version 4.48), was used to solve the coupled governing equations. However, this software requires specification of the source terms shown in Table 1 and new subroutines were written to calculate the electrochemical and permeability for this simulation. Fluent also requires a subroutine to account for the flux of protons and water across the membrane.

Figure 2 shows the geometry of the fuel cell system simulated in this work. It consists of two flow channels (upper is anode and lower is cathode) separated by diffusion layer and MEA. The flow path is ten centime-

ters long in the axial direction with a 0.1 cm (height) × 0.08 cm (width) cross-sectional area for the flow channel. Both anode and cathode flow channels are divided into 8 × 10 × 34 equally sized grid cells. Each diffusion layer has a dimension of 0.05 cm (height) × 0.16 cm (width) × 10 cm (length) and is simulated with 8 × 16 × 34 equally sized grid cells. The transport of water and protons is simulated by source terms in control volumes in contact with the membrane. The computation domain does not extend through the membrane when Equation 15 is used. A separate grid independence test was performed by increasing and decreasing the number of the grid cells. The number of grid cells were decreased and increased by 50% of the base case, and predicted results were less than 2% different from each other. We concluded that the results presented are grid independent.

Figure 3 provides an overview of the solution procedure used to solve the equations and is based on the established Simple algorithm [11]. As an initial guess for this nonlinear problem we used the inlet mole fractions and velocities throughout the channel. The three momentum equations corresponding to the x, y and z directions are solved first. Then a pressure correction equation is used to adjust the mass balance. Species transport equations are solved after these bulk flow calculations and the mixture properties for viscosity, density and diffusion in each control volume are calculated based on the local species mass fraction. The anode side gas mixture contains hydrogen, carbon dioxide and water vapour, and the cathode side gas mixture contains oxygen, water vapour and nitrogen. Therefore, density and viscosity of the two flow channels are different and they vary from one location to the other.

Two different inlet conditions are considered here based on the previous publications by Yi and Nguyen [6] and Fuller and Newman [4]. The operating pressure is 101 kPa absolute and the cell temperature is maintained at 70 °C for all cases. The present analysis considers both co- and counter-flow conditions along with the variations in the thickness of the MEA and the value of the cell voltage. In coflow, both inlets are located at the same x, whereas, in counter-flow, the two inlets are placed at opposite ends of the computation domain. Tables 3 and 4 show different flow and operating conditions used in this work. There are a total of four cases in this study and each case is divided into five subcases.

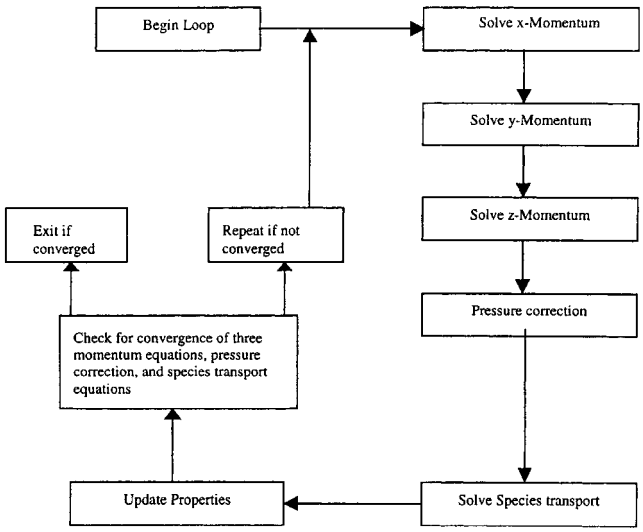

Fig. 3. Flow diagram of the solution procedure used.

Table 4 shows that in case 1.0, the operating parameters of Yi and Nguyen [6] are used. The lowest stoichiometric ratios are 2.19 and 2.18 for the anode and cathode sides, respectively. In case 1.1, the thickness of MEA is decreased by 50% from the original (127 μm) while the cell voltage is maintained at 0.53 V. In case 1.2, the membrane thickness is increased by 50% from the original with the same cell voltage. In case 1.3, the cell voltage is decreased by 50% from the original with the membrane thickness of 127 μm, and in case 1.4, the cell voltage is increased by 50% from the original with the same membrane thickness. All parameters in cases 2.0, 2.1, 2.2, 2.3, and 2.4 are similar to cases 1.0, 1.1, 1.2, 1.3 and 1.4 respectively but the flow is changed from co- to counter-flow.

The geometrical parameters of Fuller and Newman [4] and the appropriate diffusion coefficient expression are

Table 3. Inlet conditions for two base cases

		Cases similar to Yi and Nguyen [6] (cases 1 and 2)	Cases similar to Fuller and Newman [4] (cases 3 and 4)
Anode channel inlet conditions	Velocity (m s^{-1})	2.05	0.43
	Mole fraction of H_2	0.53	0.48
	Mole fraction of CO_2	0	0.16
	Mole fraction of H_2O	0.47	0.36
Cathode channel inlet conditions	Velocity (m s^{-1})	0.32	0.56
	Mole fraction of O_2	1	0.13
	Mole fraction of N_2	0	0.51
	Mole fraction of H_2O	0	0.36
Operating conditions	Permeability of diffusion layer ($\times 10^{10}$ m^2)	2	0.23

Table 4. Operating conditions for different cases

	Cases similar to Yi and Nguyen [6]											
Case	*1.0*	*2.0*	*1.1*	*2.1*	*1.2*	*2.2*	*1.3*	*2.3*	*1.4*	*2.4*		
Flow condition →	Co-flow	Counter-flow	Co-flow	Counter-flow	Co-flow	Counter-flow	Co-flow	Counter-flow	Co-flow	Counter-flow		
Membrane thickness (μm)		128		64		192		128		128		
Cell voltage (V)		0.53		0.53		0.53		0.26		0.8		
	Cases similar to Fuller and Newman [4]											
Case	*3.0*	*4.0*	*3.1*	*4.1*	*3.2*	*4.2*	*3.3*	*4.3*	*3.4*	*4.4*		
Flow condition →	Co-flow	Counter-flow	Co-flow	Counter-flow	Co-flow	Counter-flow	Co-flow	Counter-flow	Co-flow	Counter-flow		
Membrane thickness (μm)		175		87.5		263		175		175		
Cell voltage (V)		0.72		0.72		0.72		0.36		1.08		

used in case 3.0. The lowest stoichiometric ratios are 1.42 and 1.3 for the anode and cathode sides, respectively. In case 3.1, the thickness of MEA is decreased by 50% from the original 175 μm while the cell voltage is maintained at 0.72 V. In case 3.2, the membrane thickness is increased by 50% from the original with the same cell voltage. In case 3.3, the cell voltage is decreased by 50% from the original with the original membrane thickness of 175 μm, and in case 3.4, the cell voltage is increased by 50% from the original with the same membrane thickness. All parameters in cases 4.0, 4.1, 4.2, 4.3 and 4.4 are similar to cases 3.0, 3.1, 3.2, 3.3 and 3.4, respectively, but the flow is changed from co- to counter-flow.

3. Results and discussions

Results are divided into two parts: first, the results observed for flow and operating conditions similar to Yi and Nguyen [6] then the results based on operating conditions of Fuller and Newman [4] are discussed. The main differences between the two conditions are Yi and Nguyen [6] used dry and pure oxygen in the cathode stream and Fuller and Newman [4] used humid air. Moreover, the water diffusion coefficient used for Fuller and Newman [4] is greater than that used in Yi and Nguyen [6] as shown in Table 2.

3.1. *Simulation results based on operating conditions of [6], dry cathode inlet*

Figures 4 and 5 show the width-average local current density profiles along the channel length for co-flow (case 1) and counter-flow (case 2). These averaged values are calculated as an average over the width (i.e., y direction) at different axial locations. In both cases, the effects of changing the membrane thickness (Figure 4) and the cell voltage (Figure 5) are compared with Yi and

Fig. 4. Effect of membrane thickness on local width-averaged current density profiles for cases 1 and 2 comparing to the base case of Yi and Nguyen [6] (Cases: (●) 1.0, (■) 1.1, (▲) 1.2, (○) 2.0, (□) 2.1 and (△) 2.2).

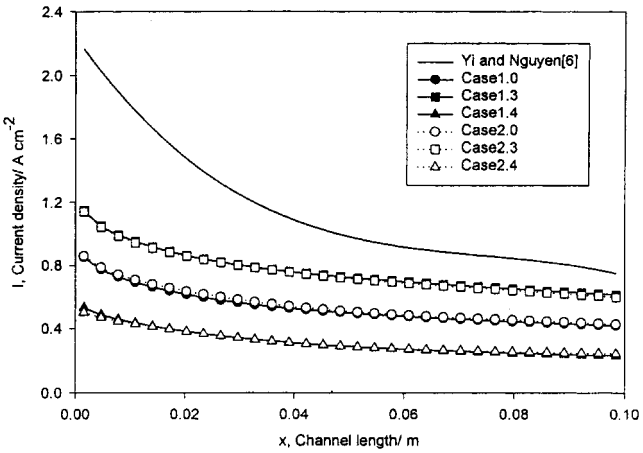

Fig. 5. Effect of cell voltage on local width-averaged current density profiles for cases 1 and 2 comparing to the base case of Yi and Nguyen [6] (Cases: (●) 1.0, (■) 1.3, (▲) 1.4, (○) 2.0, (□) 2.3 and (△) 2.4).

Nguyen's base case and they show a more uniform distribution with a diffusion layer. In Figure 4, the local current density profiles decrease with an increase in the membrane thickness (compare cases 1.0 and 2.0 with cases 1.2 and 2.2) and they increase with a decreased membrane thickness, as expected (compare cases 1.0 and 2.0 with cases 1.1 and 2.1). However, the slopes of these profiles do not change. Similarly, Figure 5 shows, the local current density is decreased when the cell voltage is increased (compare cases 1.0 and 2.0 with cases 1.4 and 2.4) and it increases with a decrease in the cell voltage (compare cases 1.0 and 2.0 with cases 1.3 and 2.3). The effect of diffusion layer creates a flow restriction and, therefore, our present calculations show lower current densities when compared to the Yi and Nguyen's base case that does not have a diffusion layer. However, since the reaction area created by diffusion layer is twice as large as the reaction area created by flow area in base case, we estimate that the total current would be about the same with the addition of the diffusion layer. In both figures, there is no significant difference in current density distribution between co- and counter-flow (case 1 and case 2). The current density is high near the hydrogen inlet and the inlet orientation of the cathode side does not significantly influence the results for this operating condition because the axial velocity on the anode side is very high (Table 1). That is the flow rates of [6] result in 268% excess hydrogen and 117% excess oxygen because their flow rates were based on a higher current.

Figure 6 shows the velocity vectors in the cross flow planes (i.e., $y-z$ plane) and the density contours for case 1.0 at $x = 0.033$ m and $x = 0.067$ m. These velocities are commonly referred to as secondary velocities and the axial velocity is known as the primary velocity. At $x = 0.033$ m and $z > 0.002$ m (i.e., the anode side), the vectors are pointing downward from the anode channel, spreading into the diffusion layer, and pointing down to the membrane surface because both species (H_2 and water vapour) are consumed on the membrane surface. Two flow mechanisms contribute to this downward secondary flow. The primary factor is that the inlet velocity is high in the anode channel, 2.05 m^{-1}. The other factor contributing to this down draft is that mass is consumed on the membrane surface due to the electrochemical reactions and the water transport across the membrane. In the cathode (i.e., $z < 0.002$ m) oxygen

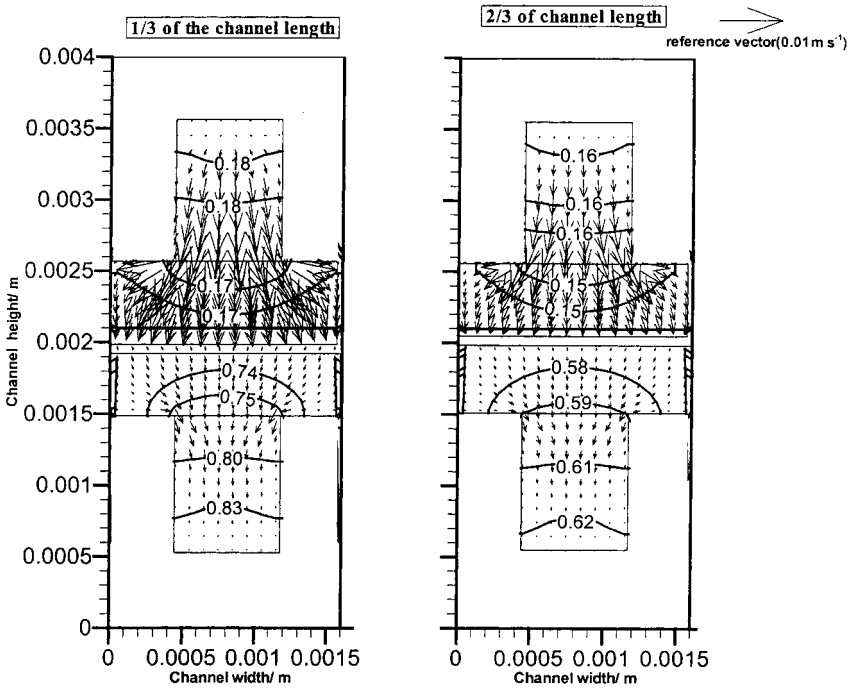

Fig. 6. Velocity vectors and mixture density contours at selected cross-flow planes for operating conditions of case 1.0 (similar to Yi and Nguyen [6]).

is consumed on the membrane surface while the water vapour is produced on the membrane surface. Here, the net velocity vectors are pointing into the cathode flow channel because the amount of water transported is more than the oxygen consumed.

The overall vector pattern indicates the total mass coming in or going out from different regions, and the contours indicate the density variations (in kg m^{-3}) of the mixture. The vectors in the upper channel at two-thirds of the axial channel show that there is a lower rate of net water transport as compared to the first one-third of the channel (i.e., 0.16 against 0.18 kg m^{-3}). It can also be observed from the density contours of the bottom channel that there is more water vapor at the downstream location. The water transport from anode to cathode decreases the anode gas-mixture density at downstream location. It is interesting to note that oxygen has to diffuse against this convective flow. Since the flow in the cathode side is away from the membrane, the oxygen needs to have a sufficient concentration gradient or diffusion effect to reach the membrane; however on the anode side of the cell, the flow of hydrogen towards the membrane benefits from the bulk flow towards the membrane.

3.2. *Simulation results based on operating conditions of [4], humidified cathode inlet*

Figures 7 and 8 show the local width-averaged current density profiles along the channel for cases 3 and 4 and they show a comparison of the effects of changing the membrane thickness (Figure 7) and the cell voltage (Figure 8) relative to Fuller and Newman's base case. It is noted that the prediction for case 3.0 shows higher current densities than predicted by Fuller and Newman [4]. Their model did not include the convection effects in the diffusion layer and it was based on a two-dimensional computation domain. Our results indicate that there are convection effects in the diffusion layer and these increase the current density. More importantly at some locations, the current density at the edges is higher than that in the channel centerline location. It should be noted that we do not impose convection, but rather with the parameters and operating conditions of this case, the equation solver determines that convection is present.

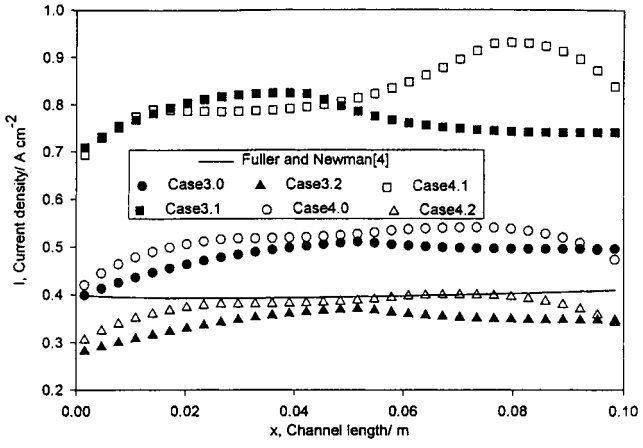

Fig. 7. Effect of membrane thickness on the local width-averaged current density profiles for cases 3 and 4 comparing to the base case of Fuller and Newman [4] (Cases: (●) 3.0, (■) 3.1, (▲) 3.2, (○) 4.0, (□) 4.1 and (△) 4.2).

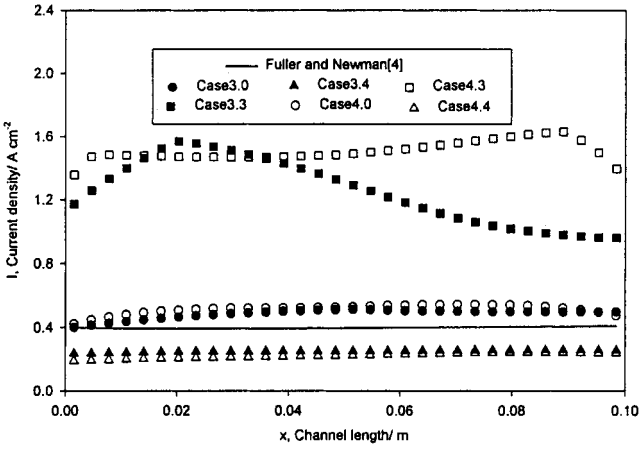

Fig. 8. Effect of cell voltage on the local width-averaged current density profiles for cases 3 and 4 comparing to the base case of Fuller and Newman [4] (Cases: (●) 3.0, (■) 3.3, (▲) 3.4, (○) 4.0, (□) 4.3 and (△) 4.4).

In Figure 7, when the membrane thickness is increased, the local current density profiles are decreased (compare cases 3.0 and 4.0 to cases 3.2 and 4.2). Similarly, decreasing the thickness of the membrane increases the local current density (compare cases 3.0 and 4.0 to cases 3.1 and 4.1). The decrease in the membrane thickness causes a substantial nonuniformity for 0.06 m $< x <$ 0.09 m for the counter flow. Figure 8 shows the effect of cell voltage changes on the local current density. The local current density is decreased with an increase in the cell voltage (compare cases 3.0 and 4.0 with cases 3.4 and 4.4), and the local current density is increased with a decrease in the cell voltage (compare cases 3.0 and 4.0 with cases 3.3 and 4.3). However, by decreasing the cell voltage, the profiles in both co- and counter-flow show an upper limiting current density.

Figure 9 shows the local current density contours for cases 3.3 and 4.3, the highest current densities in the group. The inlets and outlets marked in the figure are for the anode side and for case 4.3 the anode inlet corresponds to the cathode exit. The observed variation in current density distribution is due to water activity variations on the membrane surface rather than H_2 or O_2 limitations. The counter-flow (case 4.3) shows a more uniform current density distribution. The observed current density patterns are linked with the secondary flow patterns observed in the flow channel. For example, at 0.015 m from the inlet in case 3.3, the centerline current density is less than 1.481 A cm^{-2} and at the edges it is more than 1.481 A cm^{-2}. The secondary flow for this location is directed from the cathode channel to the anode channel and that indicates a back-diffusion of

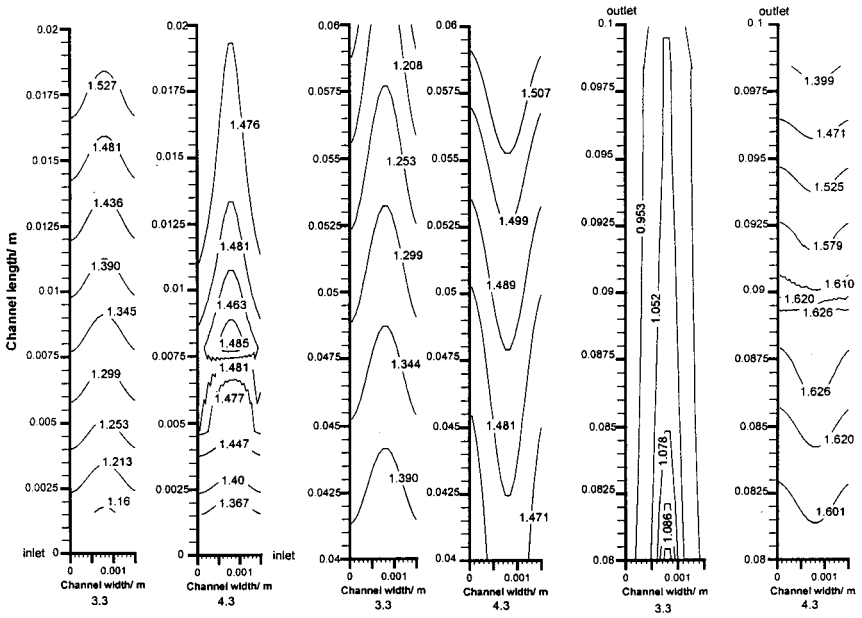

Fig. 9. Local current density $I(x, y)$ contours (A cm^{-2}) for cases 3.3 and 4.3 on the membrane surface at selected axial locations.

water. Since the path resistance for water to move from MEA surface to the flow channel is more at the edges, anode side water activity is more favorable near the edges than the centerline. Therefore, the local current density is higher at the edges than the centerline for this operating condition. However, this distribution of local current density is not the same for all locations. For example, location 0.0575 m from the inlet for the same case, the current density at the center is higher (1.253 A cm^{-2}) than the edges (less than 1.208 A cm^{-2}). Here, the secondary flow is observed to be from anode to the cathode side. Therefore, the anode side hydration of the membrane is mostly achieved by the moisture present in the anode gas stream. Since water from the gas flow path can reach the centerline location of the MEA more easily than near-edge locations, the local current density is higher at the centerline.

Figure 10 shows the secondary flow distribution in co-flow condition. Unlike the secondary flow observed with Yi and Nguyen's operating conditions, the flow can be either from anode to cathode or from cathode to anode. Near the inlet, flow is from cathode to anode as water

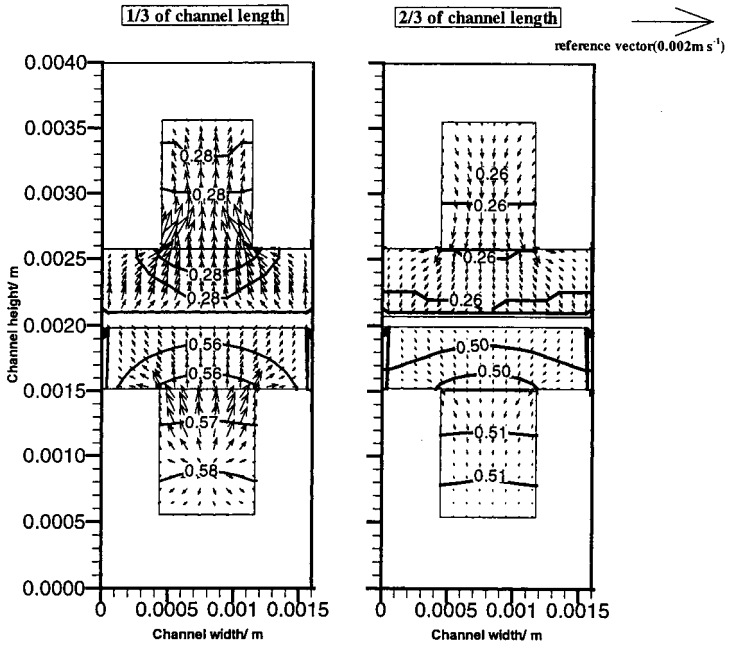

Fig. 10. Velocity vectors and mixture density contours at selected cross-flow planes for operating conditions of case 3.0 (similar to Fuller and Newman [4]).

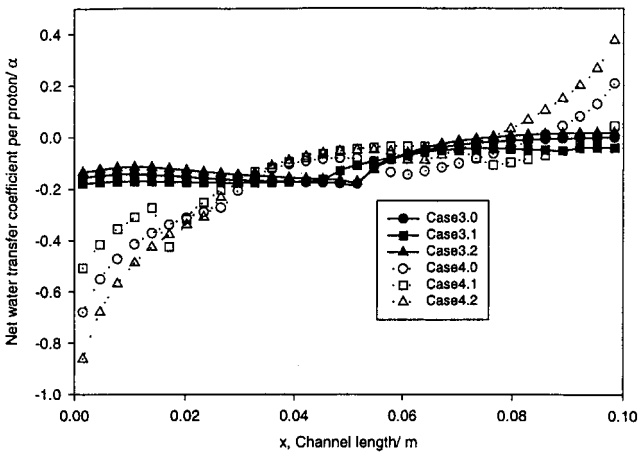

Fig. 11. Effect of membrane thickness on the width-averaged net water flux per proton (α) profiles of cases 3 and 4. (Cases: (●) 3.0, (■) 3.1, (▲) 3.2, (○) 4.0, (□) 4.1 and (△) 4.2).

diffuses through the membrane to reach the low concentration of the anode flow channel. At the 2/3 downstream location, the flow is from anode to cathode as observed in previous secondary flow of Figure 6. Regions with bulk flow from cathode to anode shows higher current densities near the edges compared to the centerline. Whereas, regions with bulk flow from anode to cathode show lower current densities near the edges compared to the centerline.

Figures 11 and 12 show that the direction of flow affects the rate of water transport or net water transfer coefficient per proton profiles. In both of these figures, a negative coefficient indicates the diffusion from the cathode to the anode is greater than the electroosmotic drag. For Figure 11, when the membrane thickness is increased (cases 3.2 and 4.2) the net water flux per proton is higher than that in cases 3.0 and 4.0. In cases 3.1 and 4.1, the rate of water transport decreases by decreasing the membrane thickness. In Figure 12, when the cell voltage is lowered (cases 3.3 and 4.3) the rate of water transport is also decreased and when the cell voltage is increased (cases 3.4 and 4.4) the rate of water transport is increased. The effects of co-flow and counter-flow create significantly different rates of water transport in each case. Co-flow creates the higher rate of water transport especially in the case of increasing cell voltage (cases 3.4 and 4.4). The effect diffusion from the cathode may be important for operation with dry anode gases.

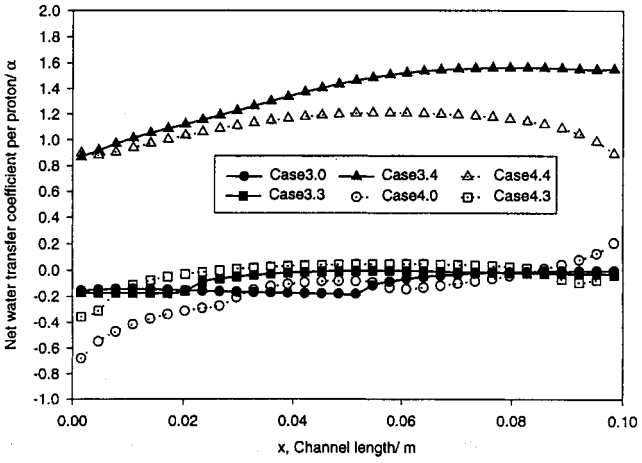

Fig. 12. Effect of cell voltage on the width-averaged net water flux per proton (α) profiles of cases 3 and 4. (Cases: (●) 3.0, (■) 3.3, (▲) 3.4, (○) 4.0, (□) 4.3 and (△) 4.4).

4. Conclusions

A three-dimensional flow simulation of PEM fuel cell has been presented. The analysis showed how to modify a commercial flow solver to include the necessary electrochemical processes. Modeled source terms can be included in any commercial flow solver and therefore, model development time will be reduced with this formulation. The addition of diffusion layers at both the anode and the cathode showed significant differences from studies that did not include these diffusion layers. The species concentrations along the flow channels were calculated. Further, the effects of the membrane thickness and the cell voltage on the local current density were presented. This work also described the mass consumption behavior by analysing the velocity distribution in cross-flow planes.

The effect of the diffusion layers added to both sides of the MEA is to create a larger reaction area. Without this layer, the reactants cannot access the MEA under the current-collector footprints. However, the diffusion layer creates a flow resistance and therefore, our study showed decreases of the local current densities relative to studies without diffusion layer. In the diffusion layer the reactants are transported by both convective and diffusive transport mechanisms and the predictions indicate that the convection effect is not negligible even for low porosity. The direction of water transport can alter the local current density distribution patterns. Water migrating from cathode to anode shows higher current densities near the edges of the computation domain and water migrating from anode to cathode shows higher current densities near the centerline. This effect can only be observed by including the width of the flow channel and gas diffusion layer in the model.

Acknowledgements

This project was supported by the Department of Energy through Cooperative Agreement Number DE-FG02-91ER75666. The authors are grateful to Professor Ralph E. White for introducing them to this research project.

References

1. J. Stumper, S.A. Campbell, D.P. Wilkinson, M.C. Johnson and M. Davis, *Electrochem. Acta* **43** (1998) 3773.

2. C. Wieser, A. Helmbold and W. Schnurnberger, Abstract 1115, Extended Abstracts for the Boston Meeting of the Electrochemical Society (Nov., 1998).
3. T.E. Springer, T.A. Zawodzinski and S. Gottesfeld, *J. Electrochem. Soc.* **138** (1991) 2334.
4. T.F. Fuller and J. Newman, *J. Electrochem. Soc.* **140** (1993) 1218.
5. T.V. Nguyen and R.E. White, *J. Electrochem. Soc.* **140** (1993) 2178.
6. J.S. Yi and T.V. Nguyen, *J. Electrochem. Soc.* **145** (1998) 1149.
7. J.S. Yi and T.V. Nguyen, *J. Electrochem. Soc.* **146** (1999) 38.
8. V. Gurau, H. Liu and S. Kakac, *AIChE J.* **44** (1998) 2410.
9. S. Shimpalee, S. Dutta, W.-K. Lee and J.W. Van Zee, paper submitted to 1999 ASME IMECE, Nashville, TN.
10. R. Bird, W. Stewart and E. Lightfoot, 'Transport Phenomena' (J. Wiley & Sons, New York, 1960).
11. S.V. Patankar, 'Numerical Heat Transfer and Fluid Flow' (Hemisphere Publishing Corp., New York, 1980.